

1 **Accumulation and subduction of buoyant material at submesoscale fronts**

2 John R. Taylor*

3 *Department of Applied Mathematics and Theoretical Physics,*

4 *University of Cambridge,*

5 *Cambridge, UK*

6 *Corresponding author address: John R. Taylor, CMS, DAMTP, University of Cambridge, Wilber-
7 force Road, Cambridge, UK, CB3 0WA.

8 E-mail: J.R.Taylor@damtp.cam.ac.uk

ABSTRACT

9 The influence of submesoscale currents on the distribution and subduction of
10 passive, buoyant tracers in the mixed layer is examined using large eddy simu-
11 lations. Submesoscale eddies are generated through an ageostrophic baroclin-
12 ic instability associated with a background horizontal buoyancy gradient.
13 The simulations also include various levels of surface cooling, which pro-
14 vides an additional source of three-dimensional turbulence. Submesoscales
15 compete against turbulent convection and re-stratify the mixed layer while
16 generating strong turbulence along a submesoscale front. Buoyant tracers ac-
17 cumulate at the surface along the submesoscale front where they are subducted
18 down into the water column. The presence of submesoscales strongly modi-
19 fies the vertical tracer flux, even in the presence of strong convective forcing.
20 The correlation between high tracer concentration and strong downwelling
21 enhances the vertical diffusivity for buoyant tracers.

22 **1. Introduction**

23 A wide range of buoyant material can be found near the ocean surface. Here, buoyant material
24 is defined as particles or droplets that move upwards relative to the surrounding water due to
25 their buoyancy. This definition includes bubbles, some types of phytoplankton, oil droplets, and
26 microplastics. Buoyant material plays an important role in air-sea gas exchange, biogeochemical
27 cycles, fisheries, and pollutant transport.

28 Buoyant material is generally not uniformly distributed across the ocean surface, but instead
29 accumulates in regions of surface convergence where it can be pulled below the surface by strong
30 downwelling currents. For example, Langmuir circulations are known to cause oil, bubbles, and
31 microplastics to accumulate in narrow rows with enhanced surface convergence and downwelling
32 (Thorpe 2000; Kukulka and Brunner 2015; Brunner et al. 2015). Downwelling of high concentra-
33 tions of buoyant material enhances the vertical flux (Veron and Melville 2001) and can significantly
34 modify the equilibrium vertical distribution of the buoyant material (Kukulka and Brunner 2015).

35 Here, turbulence-capturing large-eddy simulations (LES) are used to study the influence of
36 submesoscales on the accumulation and subduction of buoyant material. Submesoscales are
37 dynamical features characterized by horizontal scales from 0.1-10 km and a Rossby number
38 $Ro \equiv U/(fL) \sim 1$ where U and L are characteristic horizontal velocity and length scales and f
39 is the Coriolis parameter. Submesoscales have been implicated in increasing the stratification of
40 the upper ocean (Fox-Kemper et al. 2008; Mahadevan et al. 2012; Bachman and Taylor 2016;
41 Callies and Ferrari 2018) and enhancing vertical tracer fluxes (Thomas et al. 2008; Omand et al.
42 2015) while reducing the rate of turbulent mixing (Taylor and Ferrari 2011; Taylor 2016).

43 Submesoscales are often generated through a variety of ageostrophic instabilities associated
44 with large-scale currents. These instabilities include mixed layer baroclinic instability (MLI) and

45 symmetric instability (SI), which generate submesoscale flows at the expense of potential energy
46 (as for MLI) and kinetic energy (as for SI) associated with broader density fronts in thermal wind
47 balance. This represents a down-scale transfer of energy as has been confirmed by numerical
48 simulations (Capet et al. 2008).

49 The shear and horizontal convergence associated with submesoscale currents can enhance exist-
50 ing horizontal density gradients through a process known as frontogenesis. This results in ‘sub-
51 mesoscale fronts’, elongated regions with an abrupt change in density with an along-front length
52 of 0.1-10km. While frontogenesis also occurs on larger scales, the relatively large Rossby number
53 associated with submesoscale flows can lead to rapidly intensifying submesoscale fronts and gravity
54 wave generation (Shakespeare and Taylor 2014, 2015, 2016). Here, we will show that submeso-
55 scale fronts can be associated with strong surface convergence and downwelling which results in
56 accumulation and subduction of buoyant material.

57 Here, in addition to the down-scale transfer of energy from the submesoscale, small-scale turbu-
58 lence is generated by imposing a constant de-stabilizing surface heat flux which is varied between
59 four simulations. The simulations presented here do not include the effects of wind or waves. The
60 simulations do not attempt to replicate mixed layer turbulence under a certain set of realistic con-
61 ditions, but instead examine the influence of submesoscales and convection on buoyant material
62 under controlled conditions. In addition, several classes of buoyant material are modeled, each us-
63 ing a constant slip velocity (equivalent to a constant particle or droplet size). Interactions between
64 the size classes are neglected. The primary objective of this study is to examine the influence of
65 submesoscales and convection on the distribution of buoyant tracers in a controlled environment
66 with the hope that the results will motivate and guide future work under more realistic conditions.

67 2. Simulation Setup

68 The configuration of the simulations is very similar to the setup used in Taylor (2016). Specifi-
69 cally, the computational domain is 1km in each horizontal direction and 140m in the vertical. The
70 LES model solves the low-pass filtered nonhydrostatic Boussinesq Navier-Stokes equations. The
71 resolved fields are discretized on a grid with 512 points in each horizontal direction and 65 points
72 in the vertical with a constant grid spacing of 1.95m in the horizontal directions and variable grid
73 spacing ranging from 1.25m-2.87m in the vertical direction. No stress boundary conditions are
74 applied to the horizontal velocity at the top and bottom of the domain where the vertical velocity
75 is set to zero. Further details of the numerical method are available in Taylor (2016) and Taylor
76 (2008).

77 A linear equation of state is used, and potential density (or buoyancy) is treated using a single
78 scalar variable in the model. A relatively weak background density gradient is included using
79 the ‘frontal zone’ configuration used in previous studies (Thomas 2005; Taylor and Ferrari 2010;
80 Taylor 2016). Specifically, the buoyancy is decomposed according to $b_T(z, y, z, t) = b(x, y, z, t) +$
81 $M^2 x$, where b_T is the total buoyancy and M^2 is a constant background buoyancy gradient. Periodic
82 boundary conditions are then applied to b in both horizontal directions. This has the effect of
83 keeping the buoyancy difference across the domain constant. The LES model then solves the
84 following equation for b ,

$$\frac{\partial b}{\partial t} + \mathbf{u} \cdot \nabla b + uM^2 = \nabla \cdot ((\kappa + \kappa_{\text{SGS}}) \nabla b), \quad (1)$$

85 where κ is a small ‘molecular’ diffusivity, and $\kappa_{\text{SGS}}(x, y, z, t)$ is the subgrid-scale diffusivity. For
86 simplicity the subgrid-scale Prandtl number is set to unity such that $\kappa_{\text{SGS}} = \nu_{\text{SGS}}$. A small
87 constant diffusivity, $\kappa = 10^{-6} \text{m}^2/\text{s}$, is used to ensure numerical stability, although this is much
88 smaller than κ_{SGS} .

89 The initial buoyancy profile is set using a very weak stratification in the upper 60m with a buoy-
90 ancy gradient $b_z = N^2 = 9 \times 10^{-8} \text{s}^{-2}$ overlying a more stratified layer with $N^2 = 1.8 \times 10^{-6} \text{s}^{-2}$.
91 The background buoyancy gradient is held fixed at $M^2 = 3 \times 10^{-8} \text{s}^{-2}$ such that the total buoyancy
92 at $t = 0$ is

$$b_T(x, y, z, t = 0) = \int_0^z N^2(z') dz' + M^2 x. \quad (2)$$

93 The Coriolis parameter is $f = 10^{-4} \text{s}^{-1}$. As a result, the initial balanced Richardson number,
94 $Ri_B = N^2 f^2 / M^4 = 1$ and 20 in the upper and lower layers, respectively. The velocity is initialized
95 in thermal wind balance with the addition of random white noise with amplitude 10^{-6} m/s . The
96 simulation parameters are chosen such that the flow is stable with respect to SI and the most
97 unstable mode of mixed layer BCI has a wavelength approximately equal to the horizontal domain
98 size $\simeq 1 \text{ km}$ (Stone 1966; Fox-Kemper et al. 2008). The smallest unstable mode in the lower
99 layer has a wavelength larger than 4km (Stone 1966), and will therefore not be captured in the
100 simulations.

101 The simulations are forced by applying a constant surface buoyancy flux, B_0 , equivalent to cool-
102 ing the ocean surface. The magnitude of the surface buoyancy flux is varied in four simulations,
103 from $B_0 = 0$ (unforced) to $B_0 = -1.9 \times 10^{-8} \text{ m}^2/\text{s}^3$. As described in Taylor (2016), the surface
104 buoyancy flux competes with submesoscales to set the mixed layer stratification. The ratio of
105 the surface buoyancy flux to the re-stratifying submesoscale buoyancy flux associated using the
106 parameterization of Fox-Kemper et al. (2008) takes the form

$$R_{MLI} = \frac{B_0 f}{M^4 H^2}, \quad (3)$$

107 and here, R_{MLI} ranges from 0 to 0.6 (see Table 1). Note that while this definition is consistent
108 with Taylor (2016) and Callies and Ferrari (2018), when this ratio was defined in Mahadevan
109 et al. (2010, 2012), a coefficient $C_e = 0.06$ was included in the denominator and hence the values

110 of R_{MLI} are equivalent to $S = 0, 0.1, 1, 10$ in the notation of Mahadevan et al. (2012). Mahadevan
 111 et al. (2012) hypothesized that when $S < 1$, re-stratification induced by submesoscale eddies would
 112 overcome convectively-driven mixing. Hence, the chosen values of $R_{MLI} = 0.006, 0.06, \text{ and } 0.6$
 113 correspond to weak, moderate, and strong convection relative to the anticipated re-stratification.
 114 Note, however, that Taylor (2016) and Callies and Ferrari (2018) found persistent (albeit weak)
 115 stratification for $R_{MLI} \geq 0.6$.

116 In order to identify the influence of the horizontal buoyancy gradient and submesoscale dynam-
 117 ics, another set of simulations is run without a background buoyancy gradient, i.e. $M^2 = 0$ in Eq.
 118 1. Since these simulations do not start with available potential energy or thermal wind shear, and
 119 since the surface cooling is homogeneous, submesoscales do not develop. Instead, when surface
 120 cooling is applied, a statistically homogeneous convective layer develops. Since the horizontal
 121 scales associated with convection are relatively small, a smaller domain size of 250m is used in
 122 each horizontal direction, while the grid spacing is the same as in the first set of simulations. The
 123 parameters both sets of simulations are listed in Table 1.

124 Here, we use the same approach as in Kukulka and Brunner (2015) and model buoyant material
 125 as a continuous concentration of individual non-interacting particles. Each particle is assumed
 126 to move with the local fluid velocity plus an additional constant upwards ‘slip’ velocity. This is
 127 equivalent to assuming an instantaneous balance between the buoyant force and friction on the
 128 rising particle and is valid for small Stokes number and constant particle size. The equations for
 129 the concentration of buoyant material, or buoyant tracers, are

$$\frac{\partial c}{\partial t} + \mathbf{u} \cdot \nabla c + w_s \frac{\partial c}{\partial z} = \nabla \cdot ((\kappa + \kappa_{SGS}) \nabla c), \quad (4)$$

130 where w_s is a constant slip velocity and κ and κ_{SGS} are the same as introduced above in
 131 the buoyancy equation. Four tracers will be considered, with different slip velocities, $w_s =$

132 $(0, 0.05, 0.5, 5)$ mm/s. The numerical method used to solve the buoyant tracer equations is the
133 same as described above for momentum and buoyancy, except that the term involving advection
134 by the slip velocity is treated with an upwinding scheme for numerical stability. The initial condi-
135 tions for all tracers is $c(t = 0) = e^{z/d}$, where $d = 10$ m, independent of both horizontal directions
136 and normalized such that $c(z = 0, t = 0) = 1$.

137 One minor difference between the simulations here and those in Taylor (2016) is the spinup. In
138 Taylor (2016), MLI was allowed to develop until the submesoscale flow reached a finite amplitude
139 before the surface cooling was started and the phytoplankton concentration was initialized. This
140 ensured that the time needed for submesoscales to develop was the same regardless of the strength
141 of surface cooling - an important feature for comparing the biological response in each simula-
142 tion since the phytoplankton concentration grew or decayed exponentially in time. Here, since
143 the tracer concentration is conserved, this spinup period is not needed and velocity, buoyancy, and
144 buoyant tracers are initialized at the same time ($t = 0$) and the surface heat flux is constant through-
145 out the simulation. As a result, MLI develops in a mixed layer with active turbulent convection in
146 the forced simulations with $B_0 \neq 0$.

147 **3. Results**

148 *a. Flow description*

149 Figure 1(a) shows a time series of the stratification, averaged in the central portion of the mixed
150 layer, $-40\text{m} < z < -20\text{m}$, and over the full horizontal domain. MLI develops more rapidly in the
151 simulations with moderate and strong convection compared to the unforced case. Somewhat para-
152 doxically, this causes mixed layer stratification to develop sooner in the simulations with convec-
153 tion. Once stratification develops, its strength and vertical structure is very similar to that reported

154 in Taylor (2016). All time averages reported below will be calculated using a time window of one
155 day centered at the time of maximum mixed layer stratification. While somewhat arbitrary, this
156 choice ensures that submesoscales have developed before the start of the time average. The start
157 and end of the time averaging window are marked using dots in Figure 1(a).

158 Relative to homogeneous turbulent convection, submesoscale activity enhances the vertical ve-
159 locity for weak convective forcing, while suppressing the vertical velocity for stronger forcing.
160 This is shown in Figure 1(b) which shows vertical profiles of the root mean square (*rms*) vertical
161 velocity for the four simulations listed in Table 1. Here, the *rms* is calculated with respect to an
162 average in both horizontal directions, and the result is then averaged over the time intervals shown
163 in Figure 1(a). Dashed lines show simulations with the same forcing strength, but without a back-
164 ground density front, and therefore without submesoscale activity. For all forcing strengths, the
165 *rms* vertical velocity is enhanced below the mixed layer in the simulations when a background
166 density gradient is present.

167 Horizontal cross-sections of the vertical velocity at a depth of 25m illustrate the onset of convec-
168 tion and the development of a submesoscale eddy (Figure 2) for $B_0 = -1.9 \times 10^{-9} \text{m}^2/\text{s}^3$. Similar
169 features are also seen in the other forced simulations with $M^2 \neq 0$. Early times are characterized
170 by a relatively uniform field of convective cells (panel a), which then organize into inclined bands
171 (panel b). After about 2 days, the convective bands have merged to form larger features and be-
172 gin to show cyclonic roll-up in ‘comma’-like features (panel c). Finally, after about 3 days, these
173 features merge into a single cyclonic submesoscale eddy (panel d). Once it develops, the subme-
174 soscale eddy and front persist for the rest of the simulation. Intense subduction occurs along the
175 submesoscale front where small-scale turbulence is intensified, while other parts of the domain are
176 relatively quiescent.

177 *b. Buoyant tracers*

178 Figure 3(a) shows profiles of the mean turbulent tracer flux, $\langle w'c' \rangle$, for neutral and a buoy-
179 ant tracer. Here $\langle \cdot \rangle$ denotes an average in x, y and over the time windows indicated in Fig-
180 ure 1(a), and primes denote departures from the average. Solid lines indicate simulations with
181 $M^2 = 3 \times 10^{-8} \text{s}^{-2}$ and active submesoscales and dashed lines indicate simulations with $M^2 = 0$
182 and no submesoscale activity. For weak and moderate forcing, the magnitude of the tracer flux of
183 neutral tracers (figure 3a) is significantly enhanced by the presence of submesoscales. However,
184 for strong forcing ($B_0 = -1.9 \times 10^{-8} \text{m}^2/\text{s}^3$), the neutral tracer flux is very similar with and with-
185 out submesoscales. This is consistent with Taylor (2016) who found that submesoscales did not
186 significantly alter the turbulent diffusivity associated with phytoplankton for strong forcing.

187 The mean vertical fluxes for buoyant tracers with $w_s = 5 \text{mm/s}$ (figure 3b) are qualitatively
188 and quantitatively different compared to the fluxes of neutral tracers. For buoyant tracers with
189 $w_s = 5 \text{mm/s}$, the mean vertical flux associated with buoyant rise is nearly balanced by downward
190 mixing by turbulence, i.e. $w_s \langle c \rangle \simeq - \langle w'c' \rangle$. For all forcing strengths, the magnitude of the buoyant
191 tracer flux is maximum near the surface, reaching values $100\times$ larger than the maximum values
192 for neutral tracers.

193 Unlike the case for neutral tracers, submesoscales have a strong influence on the vertical flux
194 of buoyant tracers under strong forcing (compare the solid and dashed red curves in figure 3b).
195 Specifically the vertical tracer flux is more depth dependent for $M^2 = 3 \times 10^{-8} \text{s}^{-2}$ compared
196 with $M^2 = 0$ in the strongly forced simulation with $B_0 = -1.9 \times 10^{-9} \text{m}^2/\text{s}^3$. The strong depth
197 dependence in the turbulent flux of buoyant tracers is reflected in a strong depth dependence in the
198 mean tracer concentration (see figure 4).

199 In all cases the mean concentration of buoyant tracers is surface intensified, while all tracers
 200 are advected to deeper depths in simulations with stronger forcing (see figure 4). In most cases
 201 the mean tracer concentration is more uniform in the mixed layer for simulations with $M^2 = 0$
 202 (dashed lines) compared to those with $M^2 \neq 0$. This is consistent with the finding from Taylor
 203 (2016) that submesoscales suppress turbulent mixing. In all of the forced simulations, neutral
 204 and weakly buoyant tracers ($w_s = 0$ and $w_s = 0.05\text{mm/s}$) are advected deeper in the simulations
 205 with submesoscales present. In the simulation with $B_0 = -1.9 \times 10^{-9}\text{m}^2/\text{s}^3$ this difference is
 206 significant. For example, in the simulation with $M^2 = 3 \times 10^{-8}\text{s}^{-2}$, the depth where $\langle c \rangle = 0.01$ is
 207 more than 20m deeper than in the simulation with $M^2 = 0$ (figure 4c).

208 Although all tracers are advected by the same velocity field, the effective vertical diffusivity is
 209 larger for buoyant tracers. The effective vertical diffusivity can be diagnosed by taking the ratio of
 210 the diagnosed tracer flux from the LES model and dividing by the mean tracer gradient, i.e.

$$\kappa_v(z, t, c) = \frac{-\langle w'c' \rangle}{\partial \langle c \rangle / \partial z}, \quad (5)$$

211 Figure 5 shows κ_v for the simulations with $M^2 = 3 \times 10^{-8}\text{s}^{-2}$. In all cases, the diagnosed diffu-
 212 sivity for the tracer with the smallest slip velocity is very close to that for a neutral tracer (with
 213 $w_s = 0$). However, κ_v diagnosed for the tracer with the largest slip velocity can be more than a fac-
 214 tor of 10 larger than κ_v for the neutral tracer. This effect becomes less pronounced for simulations
 215 with stronger forcing, but enhancement of κ_v still occurs.

216 It is worth emphasizing that the κ_v profiles in Figure 5 are diagnosed for the same velocity
 217 fields. Smith et al. (2016) found that even neutrally buoyant passive tracers with different initial
 218 conditions experienced different levels of κ_v in the same flow field. The cause of the difference
 219 in κ_v seen here is apparent from the spatial distributions of each tracer. Figure 6 shows horizontal
 220 slices of the tracers for the simulation with $B_0 = -1.9 \times 10^{-9}\text{m}^2/\text{s}^3$ at the same time and depth as

221 shown in Figure 2d. At this depth ($z = -25\text{m}$) the neutral and weakly buoyant tracers (panels a
222 and b, respectively) are relatively well-mixed. In contrast, the concentration of the more buoyant
223 tracers is elevated near the submesoscale front where strong downwelling occurs. Non-zero con-
224 centrations of the most buoyant tracer only occur in locations coincident with strong downwelling.
225 The correlation between high tracer concentration and negative vertical velocity enhances κ_v for
226 buoyant tracers.

227 **4. Conclusions and Discussion**

228 Here, large-eddy simulations (LES) have been used to study the influence of submesoscale dy-
229 namics on buoyant tracers in the upper ocean. Small-scale turbulence is generated by imposing a
230 constant, de-stabilizing surface buoyancy flux while submesoscales are generated through mixed
231 layer instability (MLI) associated with an imposed background horizontal buoyancy gradient. A
232 submesoscale front develops around the edge of the submesoscale eddy and the front is associated
233 with enhanced small-scale turbulence and intense downwelling.

234 Buoyant tracers accumulate near the surface along submesoscale fronts driven by convergent
235 horizontal flows. Strong downwelling along the submesoscale front subducts buoyant tracers and
236 enhances the vertical diffusivity relative to a neutrally buoyant tracer. For weakly buoyant tracers
237 and/or strong convection, the tracers remain relatively homogeneous in the mixed layer, and the
238 strong correlation between submesoscale currents and tracer concentration is broken.

239 Callies and Ferrari (2018) found that submesoscale motions persist even in the presence of strong
240 buoyant convection. In the simulations here, the vertical turbulent flux associated with neutral
241 tracers under strong convective forcing is very similar with and without submesoscales, a result
242 consistent with Taylor (2016). However, the same is not true for strongly buoyant tracers. In
243 this case, submesoscale motions remain effective in accumulating buoyant tracers in regions of

244 intense downwelling. As a result, the turbulent flux of highly buoyant tracers in strong forcing is
245 significantly altered by the presence of submesoscales. This implies that persistent submesoscale
246 currents seen by Callies and Ferrari (2018) under strong convective forcing have a strong influence
247 on the transport of buoyant tracers.

248 These results present several challenges for ocean models. First, the submesoscale front where
249 buoyant tracers accumulate is less than 100m wide (see Fig. 6). Resolving fronts and filaments
250 on this scale is challenging, even for high-resolution regional ocean models. Adding to this chal-
251 lenge is the observation that buoyant tracers sample the flow field differently depending on their
252 buoyancy. Buoyant material such as oil droplets, bubbles, and micro-plastics are composed of a
253 range of particle sizes and slip velocities. Particles in different size classes would then respond
254 differently to the same flow field. This could lead to particle segregation, further complicating
255 efforts to model the response of buoyant material.

256 While these challenges might seem daunting, there are still opportunities for progress. One
257 approach would be a statistical representation of submesoscale fronts and filaments. For example,
258 it might be possible to use idealized models to describe the properties (e.g. width, depth, strength,
259 frequency of occurrence) of submesoscale fronts as a function of mesoscale properties including
260 mixed layer depth, strain, density gradients, etc. Instead of resolving individual submesoscale
261 fronts and filaments, one could represent important quantities such as the vertical flux of buoyant
262 tracers by averaging across an ensemble of characteristic submesoscale fronts and filaments and
263 more quiescent regions. Idealized simulations like those described here could help describe how
264 to weight the average depending on the buoyancy of the tracers involved.

265 **Acknowledgements**

266 This work benefited from a grant from the Gulf of Mexico Research Initiative. The author
267 is grateful for helpful comments from the CARTHE project team. Kat Smith provided helpful
268 comments and suggestions on a draft of this paper.

269 **References**

270 Bachman, S. D., and J. R. Taylor, 2016: Numerical simulations of the equilibrium between eddy-
271 induced restratification and vertical mixing. *Journal of Physical Oceanography*, **46 (3)**, 919–
272 935.

273 Brunner, K., T. Kukulka, G. Proskurowski, and K. Law, 2015: Passive buoyant tracers in the ocean
274 surface boundary layer: 2. Observations and simulations of microplastic marine debris. *Journal*
275 *of Geophysical Research: Oceans*, **120 (11)**, 7559–7573.

276 Callies, J., and R. Ferrari, 2018: Baroclinic instability in the presence of convection. *Journal of*
277 *Physical Oceanography*, **48 (1)**, 45–60.

278 Capet, X., J. C. McWilliams, M. J. Molemaker, and A. Shchepetkin, 2008: Mesoscale to subme-
279 soscale transition in the California Current System. part III: Energy balance and flux. *Journal*
280 *of Physical Oceanography*, **38 (10)**, 2256–2269.

281 Fox-Kemper, B., R. Ferrari, and R. Hallberg, 2008: Parameterization of mixed layer eddies. Part
282 I: Theory and diagnosis. *Journal of Physical Oceanography*, **38 (6)**, 1145–1165.

283 Kukulka, T., and K. Brunner, 2015: Passive buoyant tracers in the ocean surface boundary layer: 1.
284 Influence of equilibrium wind-waves on vertical distributions. *Journal of Geophysical Research:*
285 *Oceans*, **120 (5)**, 3837–3858.

286 Mahadevan, A., E. D'Asaro, C. Lee, and M. J. Perry, 2012: Eddy-driven stratification initiates
287 North Atlantic spring phytoplankton blooms. *Science*, **337 (6090)**, 54–58.

288 Mahadevan, A., A. Tandon, and R. Ferrari, 2010: Rapid changes in mixed layer stratification
289 driven by submesoscale instabilities and winds. *Journal of Geophysical Research: Oceans*,
290 **115 (C3)**.

291 Omand, M. M., E. A. D'Asaro, C. M. Lee, M. J. Perry, N. Briggs, I. Cetinić, and A. Mahade-
292 van, 2015: Eddy-driven subduction exports particulate organic carbon from the spring bloom.
293 *Science*, **348 (6231)**, 222–225.

294 Shakespeare, C. J., and J. Taylor, 2014: The spontaneous generation of inertia–gravity waves
295 during frontogenesis forced by large strain: theory. *Journal of Fluid Mechanics*, **757**, 817–853.

296 Shakespeare, C. J., and J. Taylor, 2015: The spontaneous generation of inertia–gravity waves
297 during frontogenesis forced by large strain: numerical solutions. *Journal of Fluid Mechanics*,
298 **772**, 508–534.

299 Shakespeare, C. J., and J. R. Taylor, 2016: Spontaneous wave generation at strongly strained
300 density fronts. *Journal of Physical Oceanography*, **46 (7)**, 2063–2081.

301 Smith, K. M., P. E. Hamlington, and B. Fox-Kemper, 2016: Effects of submesoscale turbulence
302 on ocean tracers. *Journal of Geophysical Research: Oceans*, **121 (1)**, 908–933.

303 Stone, P. H., 1966: On non-geostrophic baroclinic stability. *Journal of the Atmospheric Sciences*,
304 **23 (4)**, 390–400.

305 Taylor, J., 2008: Numerical simulations of the stratified oceanic bottom boundary layer. Ph.D.
306 thesis, University of California, San Diego.

- 307 Taylor, J., 2016: Turbulent mixing, restratification, and phytoplankton growth at a submesoscale
308 eddy. *Geophysical Research Letters*, **43 (11)**, 5784–5792.
- 309 Taylor, J. R., and R. Ferrari, 2010: Buoyancy and wind-driven convection at mixed layer density
310 fronts. *Journal of Physical Oceanography*, **40 (6)**, 1222–1242.
- 311 Taylor, J. R., and R. Ferrari, 2011: Ocean fronts trigger high latitude phytoplankton blooms.
312 *Geophysical Research Letters*, **38 (23)**.
- 313 Thomas, L. N., 2005: Destruction of potential vorticity by winds. *Journal of physical oceanogra-*
314 *phy*, **35 (12)**, 2457–2466.
- 315 Thomas, L. N., A. Tandon, and A. Mahadevan, 2008: Submesoscale processes and dynamics.
316 *Ocean modeling in an Eddying Regime*, 17–38.
- 317 Thorpe, S., 2000: Langmuir circulation and the dispersion of oil spills in shallow seas. *Spill science*
318 *& technology bulletin*, **6 (3)**, 213–223.
- 319 Veron, F., and W. K. Melville, 2001: Experiments on the stability and transition of wind-driven
320 water surfaces. *Journal of Fluid Mechanics*, **446**, 25–65.

321 **LIST OF TABLES**

322 **Table 1.** Simulation parameters 18

TABLE 1. Simulation parameters

L_x, L_y, L_z (m)	$\Delta x, \Delta y, \Delta z$ (m)	M^2 (s ⁻²)	f (s ⁻¹)	$B_0 \times 10^8$ (m ² /s ³)	R_{MLI}
1000,1000,140	2,2,1.3-3	3×10^{-8}	10^{-4}	(0,-0.019,-0.19,-1.9)	(0,0.006,0.06,0.6)
250,250,140	2,2,1.3-3	0	10^{-4}	(0,-0.019,-0.19,-1.9)	N/A

323 **LIST OF FIGURES**

324 **Fig. 1.** (a) Balanced Richardson number, $\langle Ri_B \rangle = \langle N^2 \rangle f^2 / M^4$, where angle brackets denote an
325 average over both horizontal directions and from $-40\text{m} < z < -20\text{m}$. Dots indicate the start
326 and end of the window used for time-averaging. (b) Vertical profiles of the root-mean-square
327 (*rms*) vertical velocity, averaged over the time interval shown in panel (a). 20

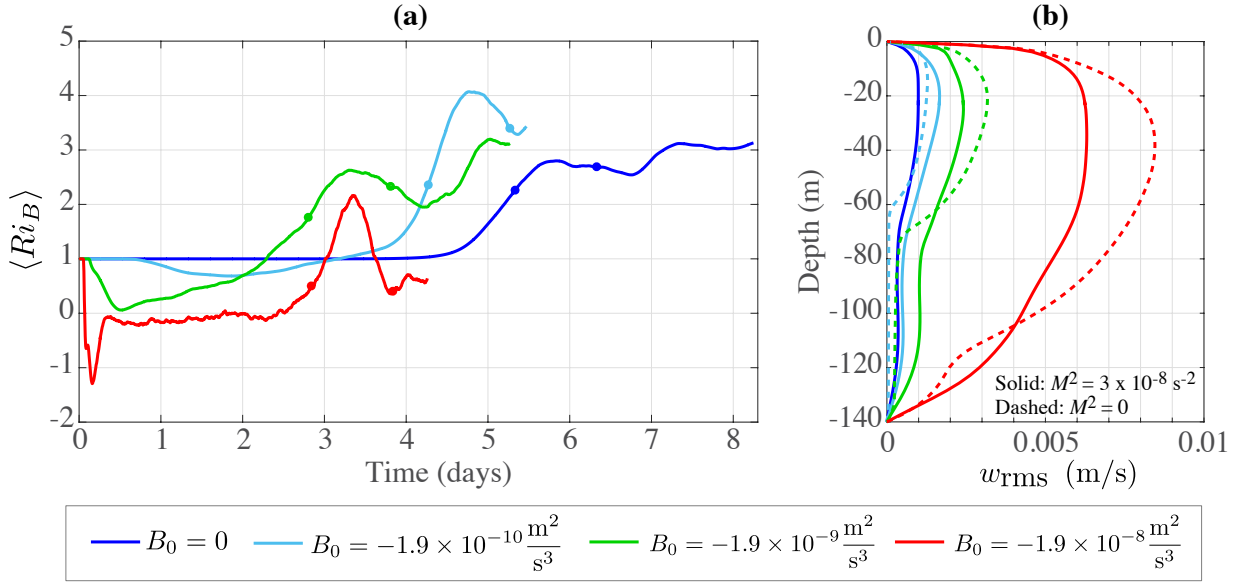
328 **Fig. 2.** Horizontal cross-sections of the vertical velocity from simulation with $M^2 = 3 \times 10^{-8} \text{ s}^{-2}$
329 and $B_0 = -1.9 \times 10^{-9} \text{ m}^2/\text{s}^3$ at $z = -25\text{m}$ 21

330 **Fig. 3.** Vertical profiles of the mean turbulent tracer flux $\langle w'c' \rangle$ for (a) neutral and (b) buoyant
331 tracers. Solid lines indicate simulations with a background horizontal density gradient of
332 $M^2 = 3 \times 10^{-8} \text{ s}^{-2}$, dashed lines indicate simulations with $M^2 = 0$ 22

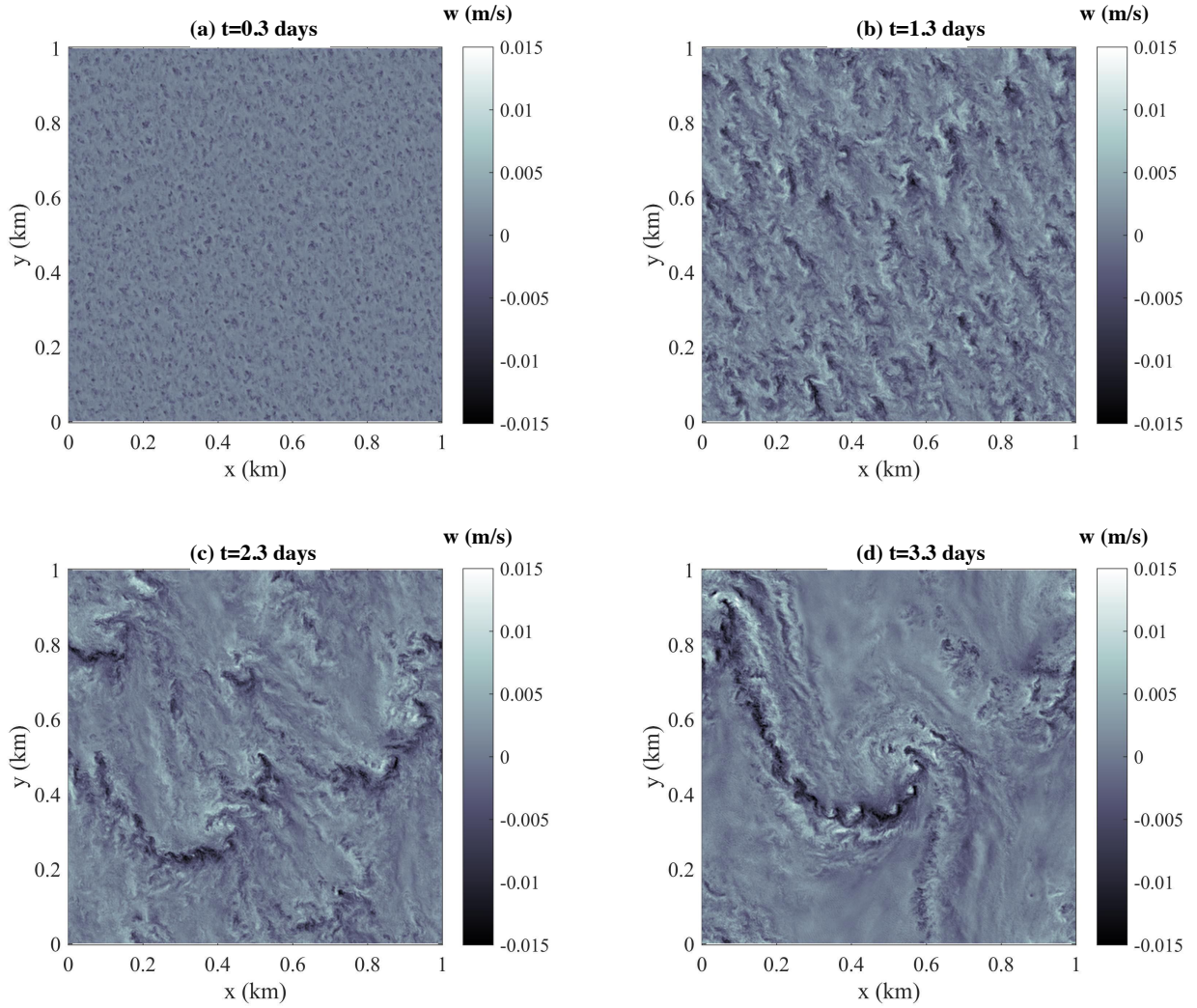
333 **Fig. 4.** Vertical profiles of the mean tracer concentrations. Solid lines indicate simulations with a
334 background horizontal density gradient of $M^2 = 3 \times 10^{-8} \text{ s}^{-2}$, dashed lines indicate simula-
335 tions with $M^2 = 0$, and dotted lines show the initial tracer concentration. 23

336 **Fig. 5.** Effective vertical diffusivity, $\kappa_v \equiv -\langle w'c' \rangle / (\partial \langle c \rangle / \partial z)$, where angle brackets denote an av-
337 erage in both horizontal directions and over the time intervals indicated in Figure 1(a). To
338 avoid numerical truncation errors, only depths where $\langle c \rangle > 10^{-6}$ are shown. Note that the
339 limits of the κ_v axis are different for panels (a-b) and (c-d). 24

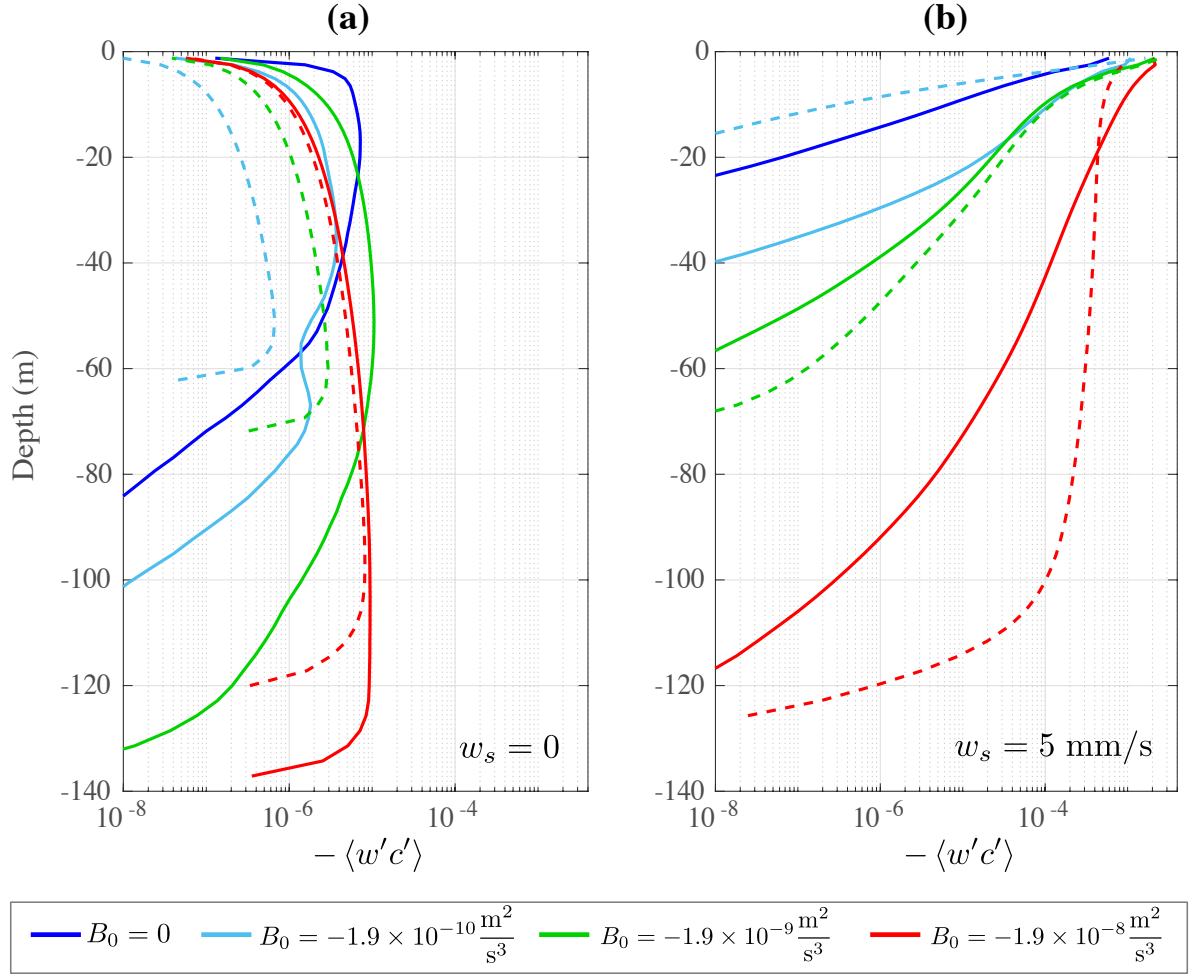
340 **Fig. 6.** Horizontal slices of various passive tracer concentrations at $z = -25\text{m}$ and $t = 3.3$ days in
341 the simulation shown in Figure 2 (compare with panel d). White contours indicate regions
342 of strong downwelling with $w = -0.005$ m/s. 25



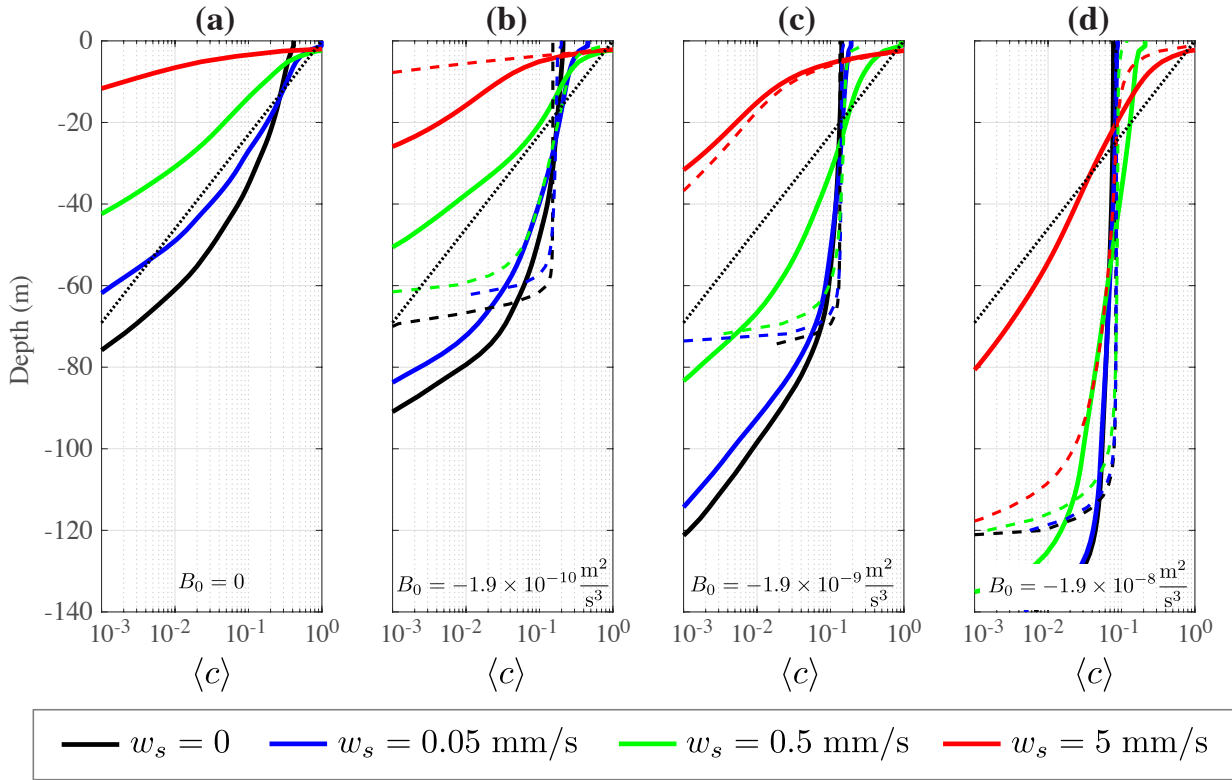
343 FIG. 1. (a) Balanced Richardson number, $\langle Ri_B \rangle = \langle N^2 \rangle f^2 / M^4$, where angle brackets denote an average over
 344 both horizontal directions and from $-40\text{m} < z < -20\text{m}$. Dots indicate the start and end of the window used
 345 for time-averaging. (b) Vertical profiles of the root-mean-square (*rms*) vertical velocity, averaged over the time
 346 interval shown in panel (a).



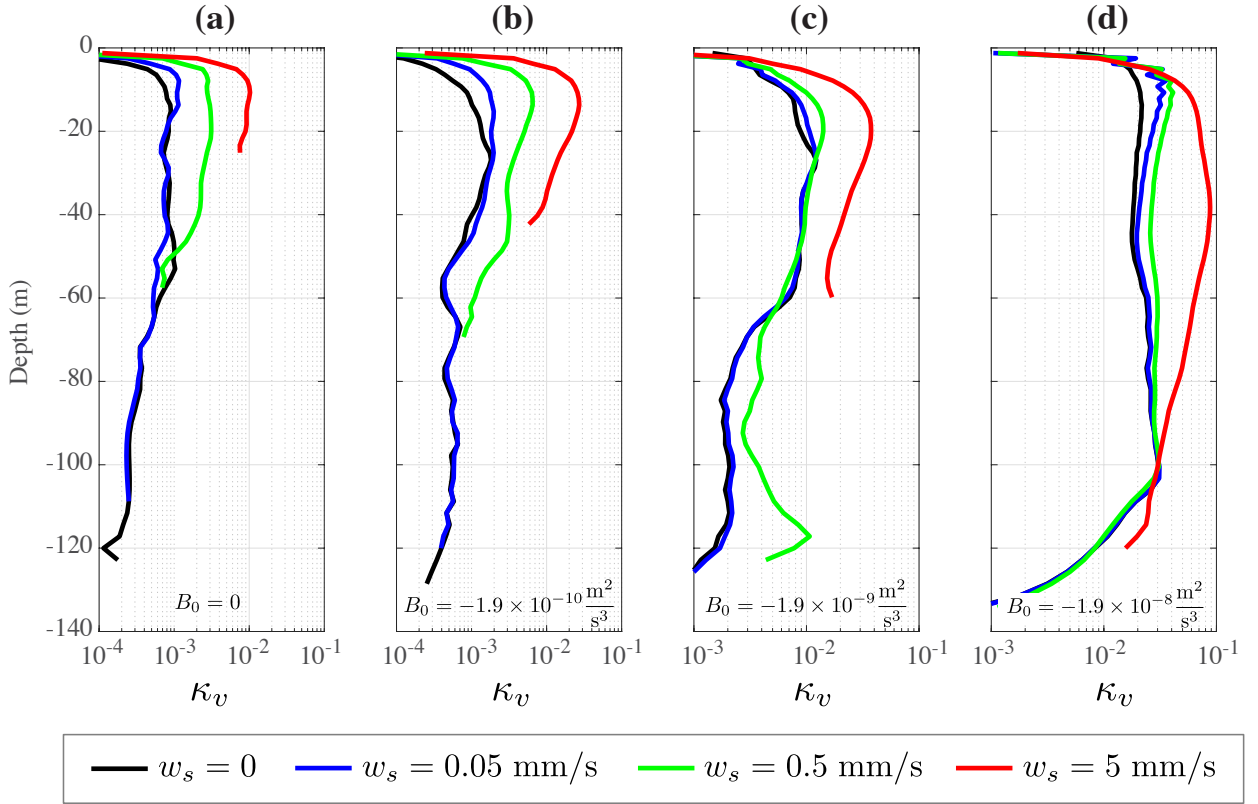
347 FIG. 2. Horizontal cross-sections of the vertical velocity from simulation with $M^2 = 3 \times 10^{-8} \text{ s}^{-2}$ and $B_0 =$
 348 $-1.9 \times 10^{-9} \text{ m}^2/\text{s}^3$ at $z = -25\text{m}$.



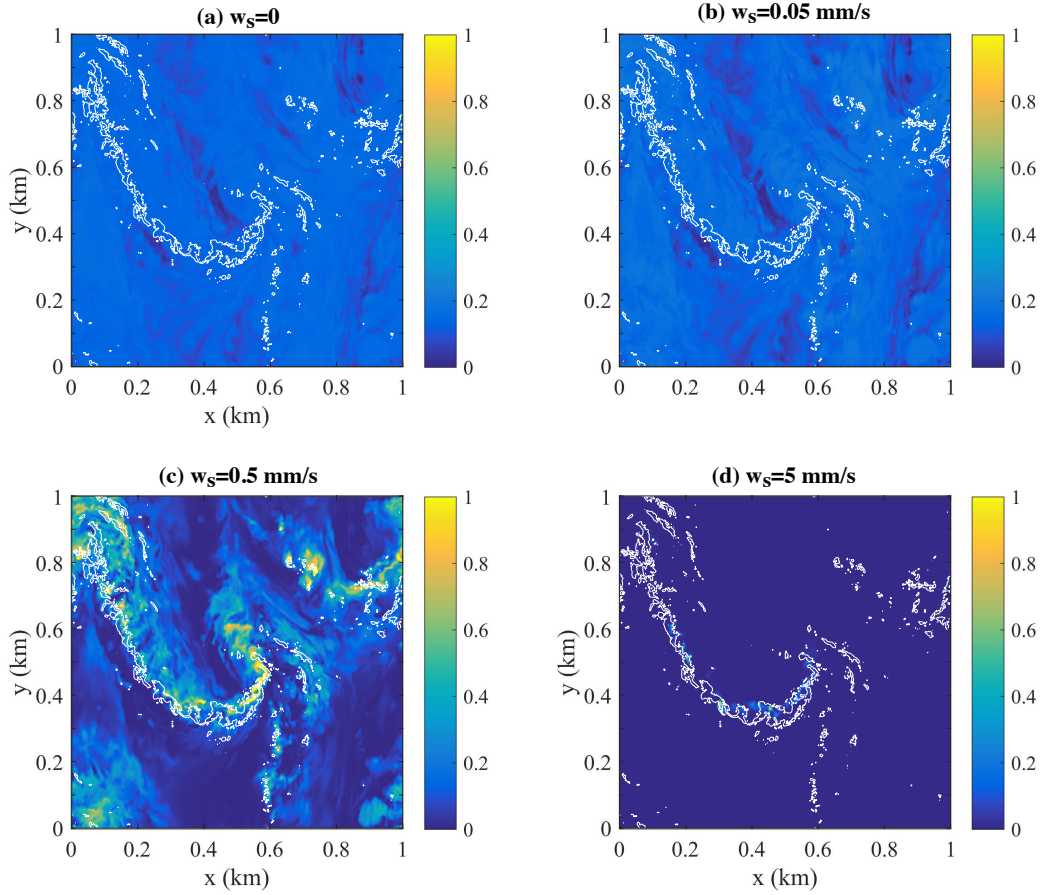
349 FIG. 3. Vertical profiles of the mean turbulent tracer flux $\langle w'c' \rangle$ for (a) neutral and (b) buoyant tracers. Solid
 350 lines indicate simulations with a background horizontal density gradient of $M^2 = 3 \times 10^{-8} \text{ s}^{-2}$, dashed lines
 351 indicate simulations with $M^2 = 0$.



352 FIG. 4. Vertical profiles of the mean tracer concentrations. Solid lines indicate simulations with a background
 353 horizontal density gradient of $M^2 = 3 \times 10^{-8} \text{s}^{-2}$, dashed lines indicate simulations with $M^2 = 0$, and dotted
 354 lines show the initial tracer concentration.



355 FIG. 5. Effective vertical diffusivity, $\kappa_v \equiv -\langle w'c' \rangle / (\partial \langle c \rangle / \partial z)$, where angle brackets denote an average in
 356 both horizontal directions and over the time intervals indicated in Figure 1(a). To avoid numerical truncation
 357 errors, only depths where $\langle c \rangle > 10^{-6}$ are shown. Note that the limits of the κ_v axis are different for panels (a-b)
 358 and (c-d).



359 FIG. 6. Horizontal slices of various passive tracer concentrations at $z = -25\text{m}$ and $t = 3.3$ days in the simu-
 360 lation shown in Figure 2 (compare with panel d). White contours indicate regions of strong downwelling with
 361 $w = -0.005$ m/s.